

X-RAY OBSERVATIONS OF THE SUPERNOVA REMNANT G21.5–0.9

S. SAFI-HARB^{1,2}

University of Manitoba, Winnipeg, MB R3T 2N2, Canada; samar@physics.umanitoba.ca

I. M. HARRUS² AND R. PETRE

NASA Goddard Space Flight Center, Greenbelt, MD 20771

AND

G. G. PAVLOV, A. B. KOPTSEVICH,³ AND D. SANWAL

Pennsylvania State University, 525 Davey Laboratory, University Park, PA 16802

Received 2001 February 13; accepted 2001 June 22

ABSTRACT

We present the analysis of archival X-ray observations of the supernova remnant (SNR) G21.5–0.9. Based on its morphology and spectral properties, G21.5–0.9 has been classified as a Crab-like SNR. For that reason, it was chosen as a *Chandra* calibration target. In their early analysis of part of these calibration data, Slane and coworkers discovered a low surface brightness, extended emission. They interpreted this component as the blast wave formed in the supernova explosion. *XMM-Newton* observations by Warwick and coworkers revealed the nonthermal nature of this emission, suggesting that it is instead an extension of the synchrotron nebula. In this paper, we revisit the *Chandra* analysis using new calibration data, improving the statistics by a factor of 2. We also include *ROSAT* and *ASCA* observations. Our analysis confirms the nonthermal nature of the extended emission. Advanced CCD Imaging Spectrometer images indicate that this component is not limb-brightened and that it shows knotty structures and a bright filament 2' north of the center. We find no evidence of line emission from any part of the remnant. We can reject a collisional equilibrium ionization thermal model at solar abundances and nonequilibrium ionization (NEI) models (such as a plane-parallel shock model with different ionization ages and constant temperature or an NEI model with a single ionization age and a constant temperature). The entire remnant is best fitted with a power-law model with a photon index steepening away from the center. The total unabsorbed flux $F_X(0.5\text{--}10 \text{ keV})$ is $1.1 \times 10^{-10} \text{ ergs cm}^{-2} \text{ s}^{-1}$ with an 85% contribution from the 40'' radius core. Timing analysis of the High-Resolution Camera data failed to detect any pulsations. We put a 16% upper limit on the pulsed fraction. We derive the physical parameters of the putative pulsar and compare them with those of other plerions (such as the Crab nebula and 3C 58).

Subject headings: ISM: individual (G21.5–0.9) — stars: neutron — supernova remnants — X-rays: ISM

1. INTRODUCTION

Crab-like supernova remnants (SNRs) have a center-brightened nebula, referred to as a plerion, often seen in the radio and X-ray wavelengths and believed to be powered by an embedded pulsar. Typified by the Crab nebula, they have nonthermal spectra and lack the evidence of an SNR shell at all wavelengths. In the radio, they are highly polarized and have a flat power-law spectral index ($\alpha \sim 0\text{--}0.3$, $S_v \sim v^{-\alpha}$). In X-rays, they have a hard photon index ($\Gamma \sim 2$, where $\Gamma = \alpha + 1$). Out of the ~ 220 Galactic SNRs, only ~ 10 candidates are classified as Crab-like SNRs.⁴

G21.5–0.9 is a plerionic SNR. In the radio, it has been imaged with the Very Large Array (VLA) at 5 GHz (Becker & Szymkowiak 1981), with the NRO Millimeter Array at 22.3 GHz, and with the Effelsberg 100 m telescope at 32 GHz (Morsi & Reich 1987). These observations show a centrally peaked highly polarized emission, of radius $\sim 40''$, having a flat radio spectral index ($\alpha \simeq 0$) and a flux density of 6 Jy at 1 GHz. The 22.3 GHz map obtained with the NRO (Fürst et al. 1988) very closely resembles the 5 GHz

map of Becker & Szymkowiak (1981; Fig. 1) and exhibits an ellipse of a 1''.5 major axis, an axial ratio of 0.8, and a position angle of $\sim 35^\circ$. The 21 cm absorption data obtained with the VLA place the SNR at a distance between 4.8 and 9.3 kpc (Becker & Szymkowiak 1981; Davelaar, Smith, & Becker 1986). Assuming a distance of 5 kpc, the linear size of the radio plerion is 2.2×1.3 pc. Fürst et al. (1988) found, in addition to the diffuse centrally peaked component, axisymmetric filaments that they interpret as signatures of jets from a central pulsar. Infrared observations of G21.5–0.9 with the ESA's *Infrared Space Observatory* Camera (ISOCAM; Gallant & Tuffs 1998) show that the plerion has a morphology similar to the 22 GHz map of Fürst et al. (1988).

X-ray observations of G21.5–0.9 point unambiguously to a centrally peaked nonthermal X-ray plerion. G21.5–0.9 was observed with the nonimaging medium-energy instrument on-board *EXOSAT*. Analysis of these data indicates a power-law spectrum with a photon index of $\Gamma = 1.72 \pm 0.12$, somewhat flatter than that of the Crab nebula (Davelaar et al. 1986). A subsequent short observation (2816 s) by *Ginga* in the 2–10 keV range could not distinguish between a power-law model with a photon index of $\Gamma = 1.88 \pm 0.05$ and a thermal bremsstrahlung model with a very high temperature $kT = 15.4 \pm 1.4$ keV (Asaoka & Koyama 1990). While the thermal bremsstrahlung yields an acceptable fit to the data, not only is the

¹ NSERC UFA fellow.

² Universities Space Research Association.

³ On leave from Ioffe Physical Technical Institute, St. Petersburg, Russia.

⁴ See D. Green's Catalog at <http://www.mrao.cam.ac.uk/surveys/snrs/>.

temperature too high, but the upper limit on the equivalent width of the Fe-K line emission (less than 0.17 keV) is too low to accommodate the expected value of emission from a plasma at cosmic abundance in ionization equilibrium. Although the properties of G21.5-0.9 suggest the presence of a pulsar, X-ray and radio imaging show no indication of a point source (Becker & Szymkowiak 1981; Kaspi et al. 1996), and all the searches for pulsation at any wavelength have proved inconclusive. G21.5-0.9 was recently observed with the *Chandra X-ray Observatory* as a calibration target. Slane et al. (2000) discovered a low surface brightness component extending to a radius of $\sim 2'$ from the central core using a 34 ks exposure with the Advanced CCD Imaging Spectrometer (ACIS-S) and a 30 ks exposure with the High-Resolution Camera (HRC-I). The authors interpret this newly discovered component as the first evidence for the expanding ejecta and blast wave formed in the initial explosion.

In this study we have carried out a combined analysis of *Chandra*, *ROSAT*, and *ASCA* data sets. We focus on the *Chandra* data, which provide the best angular resolution to date. We compile all publicly available observations by *Chandra* and present here the imaging and detailed spectral and timing analysis of a net 72 ks exposure with ACIS-S and 76 ks observation with the HRC. This allowed us to examine in more detail the spectral variations across the remnant and put a more stringent upper limit on the pulsed fraction from the yet undetected pulsar. With the longer exposure with ACIS, we detect the low surface brightness, extended component (referred to as the “shell” in Slane et al. 2000) out to a radius of 2.5 and rule out its thermal interpretation. We conclude that the spectrum of the entire remnant is dominated by nonthermal emission. The broadband images, the hardness ratio map, and the spectral properties of the remnant indicate that the entire X-ray emission could be due to synchrotron radiation from high-energy electrons injected by the “hidden” pulsar in the form of either a wind or jets interacting with the surrounding medium. We discuss our interpretation in comparison with the high-resolution 22.3 GHz observations and compare the parameters of the G21.5-0.9 plerion to the well-studied Crab and 3C 58 plerions. While G21.5-0.9 bears similarities to plerions, it has unique properties that makes it an intriguing object. To date, it is the only plerion whose X-ray size is bigger than in the radio. Its study is important to shed light on plerions of the “second kind,” a subclass of plerions having a spectral break at millimeter wavelengths (Woltjer et al. 1997). The paper is organized as follows: In the following section, we describe the observations. We describe our imaging analysis in § 3 and the corresponding spectral analysis in § 4. In § 5, we present the results of our timing analysis. Finally, we discuss our results in § 6.

2. OBSERVATIONS

2.1. Chandra

Because of its power-law spectrum, small size, and relative brightness (its unabsorbed flux is $\sim 4.3 \times 10^{-11}$ ergs $\text{cm}^{-2} \text{s}^{-1}$ between 0.4 and 2.0 keV), G21.5-0.9 was selected as one of the calibration targets of the *Chandra* observatory (Weisskopf, O’dell, & van Speybroeck 1996). As such, the SNR was observed in many configurations chosen by the instrument teams. In the following analysis, we have

made use of these different configurations to probe different aspects of the remnant. Because the CTI problems⁵ with the front-illuminated chips make it hard to perform accurate energy cuts on the data, we have not used any data from the ACIS-I, even for imaging purposes (the spatial resolution of about 1" of the damaged CCDs is still intact).

For the spectral analysis, we used six observations (ObsID 159, 1230, 1433, 1716, 1717, and 1718) corresponding to a total exposure time of 71.6 ks and obtained with ACIS-S3 (back-illuminated chip), for which the most accurate calibration exists at this point. High-resolution imaging and timing analyses were done using both the HRC-I and HRC-S and their unparalleled angular resolution.

2.2. ROSAT and ASCA

G21.5-0.9 was observed with the *ROSAT* observatory using both the Position Sensitive Proportional Counter (PSPC) and the High-Resolution Imager (HRI). Both observations are public,⁶ and although they are quite short (7.2 ks for the PSPC and 4.7 ks for the HRI), we use the PSPC data in the following analysis to better constrain the value of the column density and the HRI data to compare with the images extracted from the *Chandra* data sets.

G21.5-0.9 was also observed by both the Solid-State Imaging Spectrometer (SIS) and the Gas Imaging Spectrometer (GIS) on-board *ASCA*, and the data are also available through the HEASARC database. The exposure time is 28 ks with the GIS and 24 ks with the SIS. Because of the relatively poor angular resolution (3') of the *ASCA* X-ray telescopes, none of the fine spatial structures of G21.5-0.9 can be studied with either the GIS or the SIS. *ASCA* advantages reside in the large number of counts collected and the GIS timing capabilities (a timing resolution of 6.1×10^{-5} s for the high bit rate mode in which the data were taken). We have used the spectral analysis of the *ASCA* data sets as a measure of the “average” spectrum from the remnant to complement that extracted from the *ROSAT* PSPC and in combination with that of *Chandra*, which is the focus of this paper.

3. IMAGING

We have screened the ACIS-S data by running FSELECT on the primary events files. Only events with standard *ASCA* grades 02346 are retained. We rejected columns that lie on the edges of readout node areas and where event selection will not operate correctly since the charge cloud is split between two different readout nodes. We rejected the hot columns and pixels that are listed on the *Chandra* X-ray Center web site.⁷ We have extracted images of G21.5-0.9 in different energy bands. The images are centered at R.A. (J2000) = $18^{\text{h}}33^{\text{m}}33\overset{\text{s}}{.}50$, decl. (J2000) = $-10^{\circ}34'6\overset{\text{s}}{.}6$. In Figure 1, we show the soft- (0.1–6 keV) and hard- (6–10 keV) band images, smoothed with a Gaussian with $\sigma = 3''$. While the extended component is evident in the soft-band image, only the inner core is left in the hard band. The inner core has an angular radius of 40'', similar to the radio plerion. We refer to this component as the inner core throughout the paper. The extended component

⁵ See <http://cxc.harvard.edu/cal/Links/Acis>.

⁶ Data are available through the High Energy Astrophysics Science Archive Research Center (HEASARC) at <http://heasarc.gsfc.nasa.gov>.

⁷ See <http://asc.harvard.edu/cal/Links/Acis>.

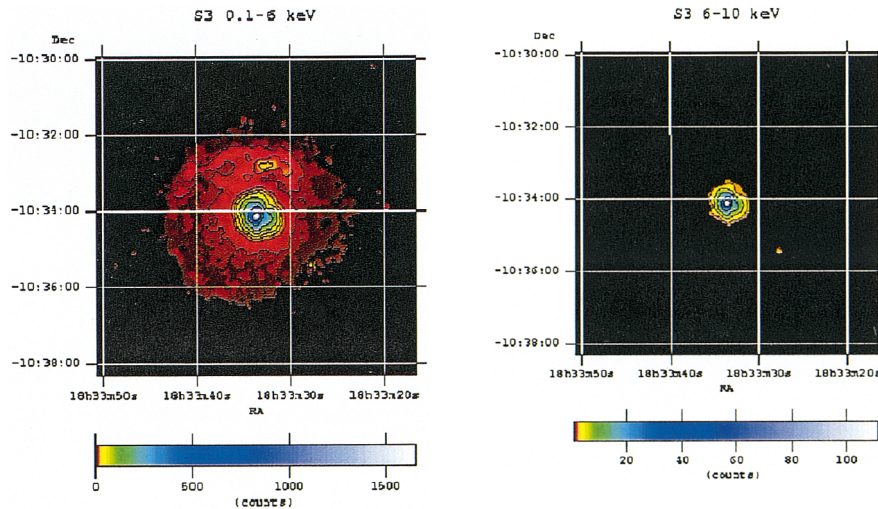


FIG. 1.—*Chandra* ACIS-S images of G21.5–0.9 at 0.1–6.0 keV (top panel) and 6.0–10.0 keV (bottom panel). The total exposure time is 71.6 ks. The images are smoothed with a Gaussian with $\sigma = 3''$. Coordinates are J2000.

extends out to a radius of 150'', slightly bigger than previously reported (120''; Slane et al. 2000), and is confirmed by *XMM-Newton* (Warwick et al. 2001). We refer to this component (50''–150'') as the low surface brightness extended component throughout the paper.

In Figure 2, we show the hardness ratio map using the ratio 2.4–10 over 0.5–2.4 keV. The image is smoothed with a Gaussian with $\sigma = 3''$. It is evident from the image that the central core is harder than the extended component. Moreover, the extended component is harder in the northern quadrant, with brighter knots and filamentary structures extending from the core out to the outer part of the SNR.

This result is consistent with the detailed spectral analysis described in § 4.1.

In Figure 3, we show the ACIS-S3 image in the 0.5–2.4 keV band with the *ROSAT* HRI contours overlaid. We smooth the *Chandra* image with a Gaussian with $\sigma = 6''$ to match the angular resolution of the HRI. The HRI image reveals the $\sim 40''$ radius inner core detected in the radio. The extended component is detected with ACIS out to a radius of 150''. The pointlike source southwest of the plerion coincides with an emission line star, SS 397.

G21.5–0.9 was observed five times with the HRC-I for a total of more than 100 ks. Unfortunately, two of those

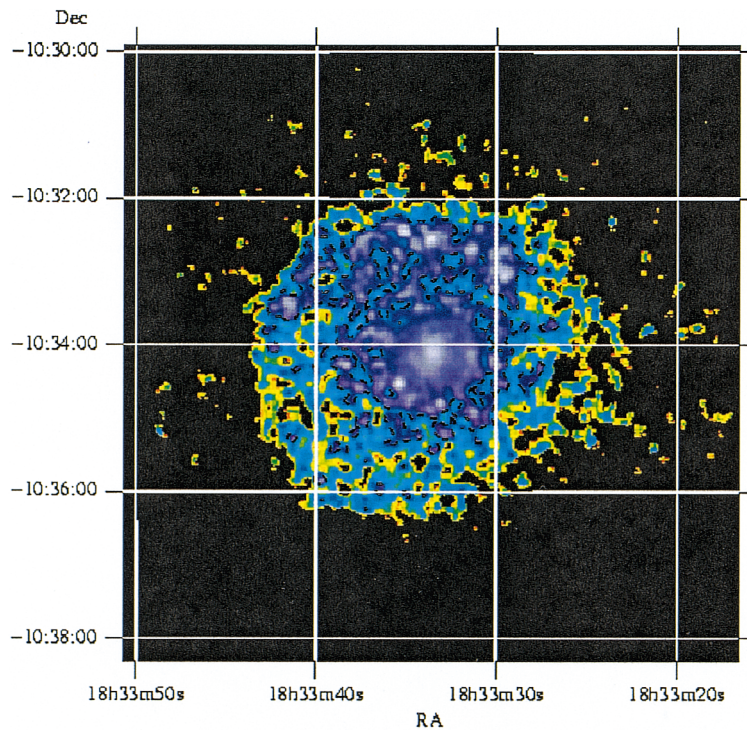


FIG. 2.—Hardness ratio map of G21.5–0.9 observed with *Chandra* ACIS-S. The ratio is 2.4–10 keV over 0.5–2.4 keV. The image is smoothed with a Gaussian with $\sigma = 3''$.

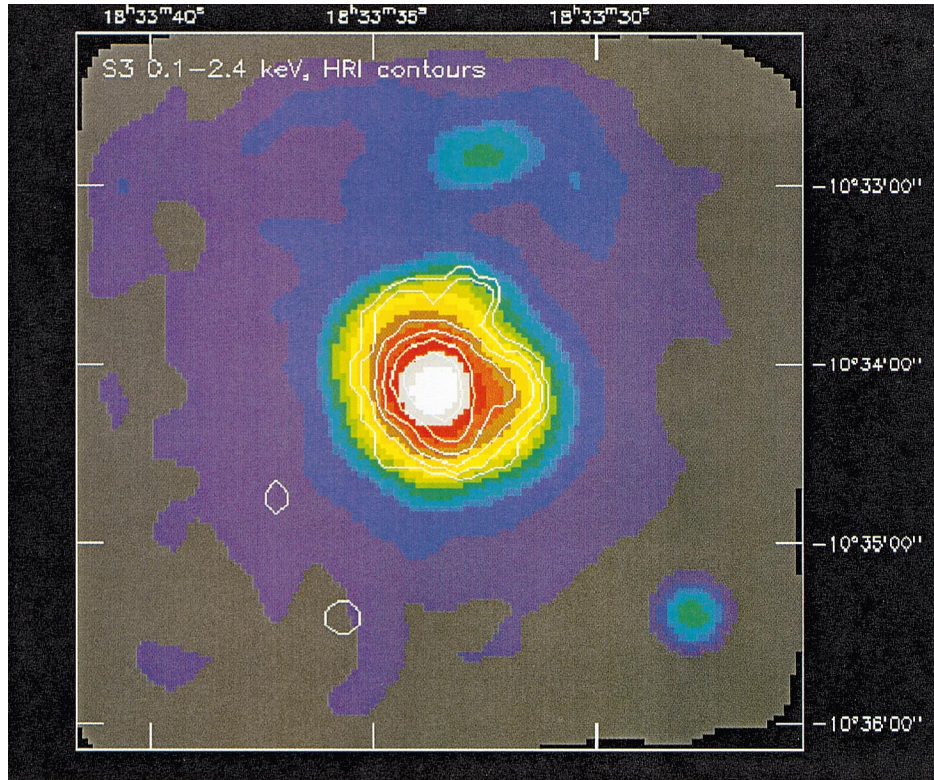


FIG. 3.—*ROSAT* HRI contours of G21.5–0.9 showing the plerion ($R \sim 40''$) overlaid on the soft-band image obtained with ACIS-S3. The pointlike source southwest of the plerion coincides with an emission-line star, SS 397. Both the HRI and ACIS-S3 images are smoothed with a Gaussian with $\sigma = 6''$ and contours are displayed in a log scale.

observations were unusable because of processing or reconstruction problems. We have used the three remaining observations and produced an image using a mosaic program that takes into account the difference in pointing. The background is subtracted using a script “screen_hrc” made available by the HRC Calibration team.⁸ This procedure flags events with a non-X-ray charge cloud distribution and removes about 30%–40% of the background events while removing only a few percent of real events. We use this script and find that 33% of events are cut, leaving a total of about 3×10^6 events. We do not correct for exposure. The result is shown in Figure 4. The image has been convolved with an elliptical top-hat filter whose size varies to have a minimum of 16 counts under the filter. The pixel size is $0''.15$. We find that the center of the HRC emission is located at R.A. (J2000) = $18^{\text{h}}33^{\text{m}}33\overset{\text{s}}{.}51(\pm 0.01)$, decl. (J2000) = $-10^{\circ}34'8\overset{\text{s}}{.}47(\pm 0.15)$. We did not measure the spectral difference across the different parts of the HRC-I emission because of the lack of spectral response in the HRC.

In Figure 5, we show the background-subtracted radial profile of the plerion obtained with HRC and ACIS. We choose the observations with minimal offsets from the telescope axis, for which a $0''.5$ radius aperture encircles 90% of the point-source counts. We note that while the ACIS profile is shown out to a radius of $\sim 100''$, the HRC profile extends to a radius of $40''$ only because of the high back-

ground at larger radii. In the inset, we show the HRC profile with $0''.25$ bins along with the expected point-spread function (PSF; dashed line). This shows that the brightest inner core is not a point source and that the brightness drops

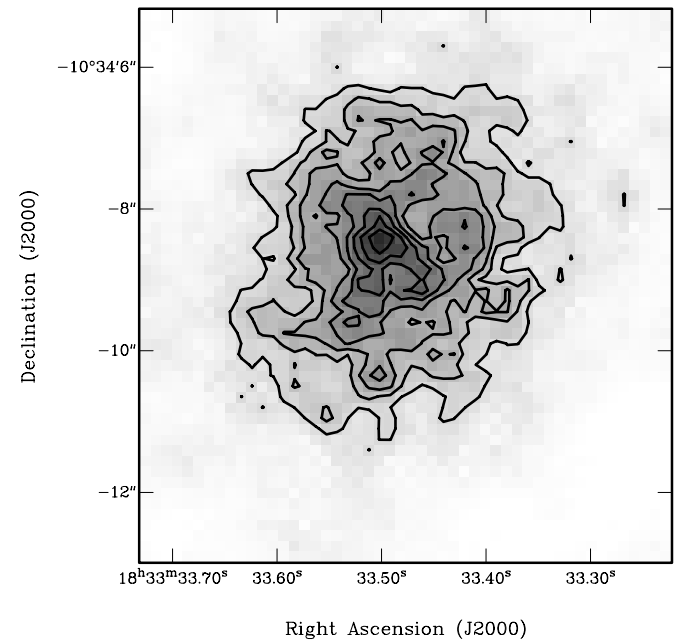


FIG. 4.—HRC-I image of the inner core of G21.5–0.9. See § 3 for details.

⁸ See <http://asc.harvard.edu/cal/Links/Hrc/CIP/filter.html>.

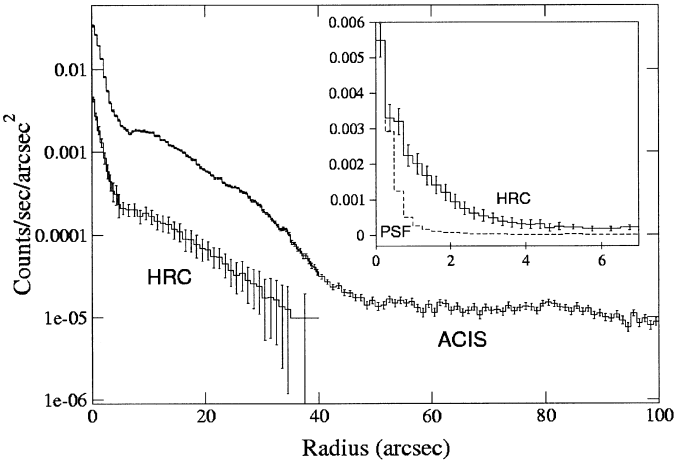


FIG. 5.—Radial profile of G21.5–0.9 using HRC and ACIS. The HRC profile extends out only to a radius $\sim 40''$ since the background dominates at larger radii. The inset shows the HRC profile with $0''.25$ bins and the expected PSF (dashed line).

sharply beyond a radius of $\sim 0''.5$. We use this profile later (§ 6.2) to infer the luminosity of the putative pulsar in G21.5–0.9.

4. SPECTRAL ANALYSIS

4.1. ACIS-S

In the following sections, we present the spectral analysis of the SNR and examine the spectral variations on the arcsecond scale. For the inner $40''$ core, we extract spectra from concentric rings of width $5''$ and centered at R.A. (J2000) = $18^{\mathrm{h}}33^{\mathrm{m}}33\overset{\mathrm{s}}{.}5$, decl. (J2000) = $-10^{\circ}34'6\overset{\mathrm{s}}{.}6$. We also extract the spectrum of the brightest $1''$ radius central part of the image. For the extended component, we extract a spectrum of a ring extending from $50''$ to $150''$ —the latter value defines the outer boundary detected with *Chandra*.

The background is extracted from the same detector region on the S3 chip using an observation of G21.5–0.9 obtained with the four ACIS-I chips and two ACIS-S chips activated. This method allows one to account for both the chip and sky background. The background-subtracted count rates in the 0.5–10 keV energy range are 2.544 ± 0.008 and 0.506 ± 0.005 counts s^{-1} from the inner core and the extended component, respectively. We processed the data as described in § 3. We used the CIAO Version 1.1 “mkarf” tool in order to generate the corresponding ancillary response files. The innermost $1''$ radius core has a very hard spectrum and is best described by a power-law model with $\Gamma = 1.4 \pm 0.1$ [$N_{\mathrm{H}} = (2.1 \pm 0.1) \times 10^{22} \mathrm{cm}^{-2}$] and an unabsorbed flux in the 0.5–10 keV range of $3.5 \times 10^{-12} \mathrm{ergs cm}^{-2} \mathrm{s}^{-1}$. We subsequently fit all the spectra simultaneously with a power law and find that the power-law index steepens with increasing radius. When allowing N_{H} to vary, we get an acceptable fit ($\chi^2_v = 0.68$, $v = 4451$) with the photon index increasing from 1.62 ± 0.05 at the inner $5''$ circle [$N_{\mathrm{H}} = (2.37 \pm 0.08) \times 10^{22} \mathrm{cm}^{-2}$] to 2.36 ± 0.07 at the outer ring [$N_{\mathrm{H}} = (1.83 \pm 0.07) \times 10^{22} \mathrm{cm}^{-2}$]. The variation of N_{H} across the plerion could be an artifact of the spectral fitting. When tying N_{H} , we get acceptable fits for all the spectra ($\chi^2_v = 0.71$, $v = 4459$), with $N_{\mathrm{H}} = (2.24 \pm 0.03) \times 10^{22} \mathrm{cm}^{-2}$ (a value consistent with that found by Warwick et al. 2001) and Γ varying from 1.53 ± 0.03 (inner $5''$ core) to

2.73 ± 0.04 (the extended component). All errors throughout the paper are at the 90% confidence level. We shall accept this value as the N_{H} for the SNR, with an uncertainty we shall determine by the range of values we find for fits to other data sets below. In Figure 6, we plot the corresponding photon index as a function of radius (with $N_{\mathrm{H}} = 2.24 \times 10^{22} \mathrm{cm}^{-2}$). The steepening of the photon index with increasing radius has been noted by Slane et al. (2000) when fitting the inner $40''$ core. Slane et al. (2000) did not, however, rule out a thermal model for the extended component and interpret that component as the SNR shell or shocked ejecta. With this longer *Chandra* observation, we find that thermal models are unlikely, as discussed further below.

In Table 1, we summarize the result of fitting the extended component with thermal and nonthermal models in the 0.6–8 keV energy range. A power-law model gives the best fit with the following parameters: $N_{\mathrm{H}} = 1.83^{+0.07}_{-0.06} \times 10^{22} \mathrm{cm}^{-2}$, $\Gamma = 2.36^{+0.07}_{-0.06}$, and $\chi^2_v = 1.0$ ($v = 658$; see Table 1). When freezing N_{H} to $2.24 \times 10^{22} \mathrm{cm}^{-2}$ (above paragraph), we get $\Gamma = 2.73 \pm 0.04$ and $\chi^2_v = 1.0$ ($v = 659$). When fitting the extended component with thermal models, we use the new models invoked in XSPEC Version 11.0.1.⁹ We can reject a collisional equilibrium ionization (CEI) model (which describes a plasma in ionization equilibrium) with solar abundances. In Figure 7, we show the spectrum of the extended component fitted with a power-law (*left-hand panel*) and Astrophysical Plasma Emission Code (APEC) model (*right-hand panel*). The latter model is the new code of thermal plasma including updated atomic lines.¹⁰ It is clear that the APEC model overestimates the data in the Fe-K line region. A very low Fe abundance is required to get an acceptable fit with the following parameters: $N_{\mathrm{H}} = 1.46 \times 10^{22} \mathrm{cm}^{-2}$, $kT = 4.1 \mathrm{keV}$, $\mathrm{Fe} = \mathrm{Ni} = 0$ (≤ 0.16 , 2σ), and $\chi^2_v = 0.96$ ($v = 657$). While the fit is formally acceptable, the derived N_{H} is inconsistent with that of the SNR. We have subsequently fitted the extended component with nonequilibrium ionization (NEI) models, which are more appropriate for modeling SNRs whose age

⁹ See <http://heasarc.gsfc.nasa.gov/lheasoft/xanadu/xspec>.

¹⁰ See <http://hea-www.harvard.edu/APEC>.

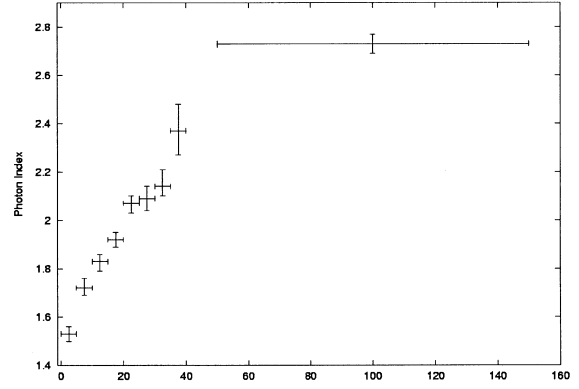


FIG. 6.—Power-law photon index Γ as a function of radius (in arcseconds). Zero radius corresponds to the brightest emission region of the plerion, centered at R.A. = $18^{\mathrm{h}}33^{\mathrm{m}}33\overset{\mathrm{s}}{.}50$, decl. = $-10^{\circ}34'6\overset{\mathrm{s}}{.}6$ (J2000). We show the power-law index of the inner $40''$ radius core (in radial increments of $5''$) and the extended component ($50''$ – $150''$) for $N_{\mathrm{H}} = 2.24 \times 10^{22} \mathrm{cm}^{-2}$.

TABLE 1
SPECTRAL PARAMETERS OF THE FITS TO THE LOW SURFACE BRIGHTNESS EXTENDED COMPONENT USING ACIS-S3 OBSERVATIONS

Model	$N_{\text{H}}^{\text{a}} (\times 10^{22} \text{ cm}^{-2})$	Model Parameter	Normalization ($\times 10^{-3}$)	χ^2_{ν} (v)
Power-Law.....	1.83 (1.77–1.90)	$\Gamma = 2.36$ (2.30–2.43)	4.36 (4.04–4.78)	1.0 (658)
APEC ^b	1.63 (1.58–1.69)	$kT = 3.33$ (3.14–3.54) keV	8.22 (7.89–8.59)	1.15
PSHOCK	1.53 (1.48–1.57)	$kT = 3.50$ (3.28–3.74) keV $\tau = 1.1 [(0.8–1.3) \times 10^9] \text{ cm}^{-3} \text{ s}^{\text{c}}$	9.72 (9.23–10.2)	0.86 (657)

NOTE.—The ranges are at the 90% confidence level.

^a Best-fit values are indicated. When freezing N_{H} to $2.2 \times 10^{22} \text{ cm}^{-2}$, the power-law model gives $\Gamma = 2.73 \pm 0.04$ ($\chi^2_{\nu} = 0.98$; v = 659), and thermal models are rejected ($\chi^2_{\nu} \sim 1.5$).

^b Assuming solar abundances (see <http://hea-www.harvard.edu/APEC>).

^c The ionization timescale $n_e t$, where n_e is the postshock electron density and t is the age of the shock.

is smaller than the time required to reach ionization equilibrium. We use the PSHOCK model (Borkowski, Leyerly, & Reynolds 2001), which comprises a superposition of components of different ionization ages appropriate for a plane-parallel shock. This model is characterized by the constant electron temperature T_e and the shock ionization age $n_e t$ (where n_e is the postshock electron density and t is the age of the shock). This model yields an adequate fit but with an unusually low ionization timescale and again a very low value of N_{H} . The parameters are $N_{\text{H}} = 1.53(1.48–1.57) \times 10^{22} \text{ cm}^{-2}$, $kT_s = 3.50$ (3.28–3.74) keV, $n_e t = 1.1(0.8–1.3) \times 10^9 \text{ cm}^{-3} \text{ s}$, and $\chi^2_{\nu} = 0.86$ (v = 657). We summarize these results in Table 1. When fitting with the NEI model, which is characterized by a constant temperature and a single-ionization timescale, we find a similar result to the PSHOCK model. Varying the abundances of Mg, Si, S, Fe,

and Ni (tied to Fe), the PSHOCK and NEI models yield a much higher $n_e t$ ($\sim 10^{12} \text{ cm}^{-3} \text{ s}$) but require unusually low abundances. These models mimic the CEI model with low abundances. We conclude that while thermal NEI models give adequate fits, they either require an unusually low $n_e t$ (with solar abundances) or, alternatively, a large $n_e t$ with unusually low metal abundances. Furthermore, the derived N_{H} from any thermal model is inconsistent with that derived for the inner core. To account for a change of $\delta(N_{\text{H}}) \geq 0.5 \times 10^{22} \text{ cm}^{-2} \sim \int n_e dl$, an unrealistic local electron density of $n_e \geq 10^3 \text{ cm}^{-3}$ is needed for a path $l \sim 2.4 \text{ pc}$ (the extent of the extended component).

We subsequently examined the spectral variations across the SNR. For that purpose, we extracted spectra from the brightest knots 2' north of the core, the northeastern edge of the SNR, and an inner circle southeast of the inner core.

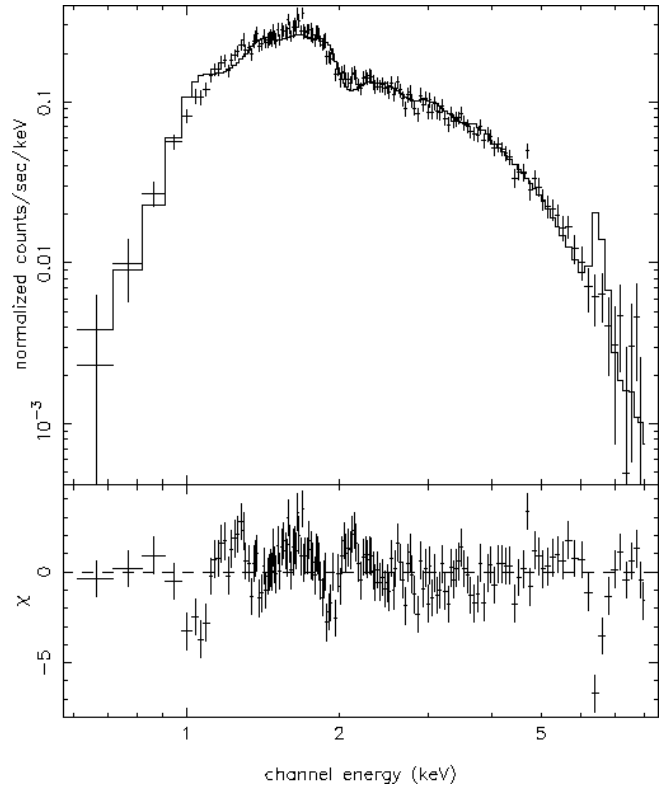
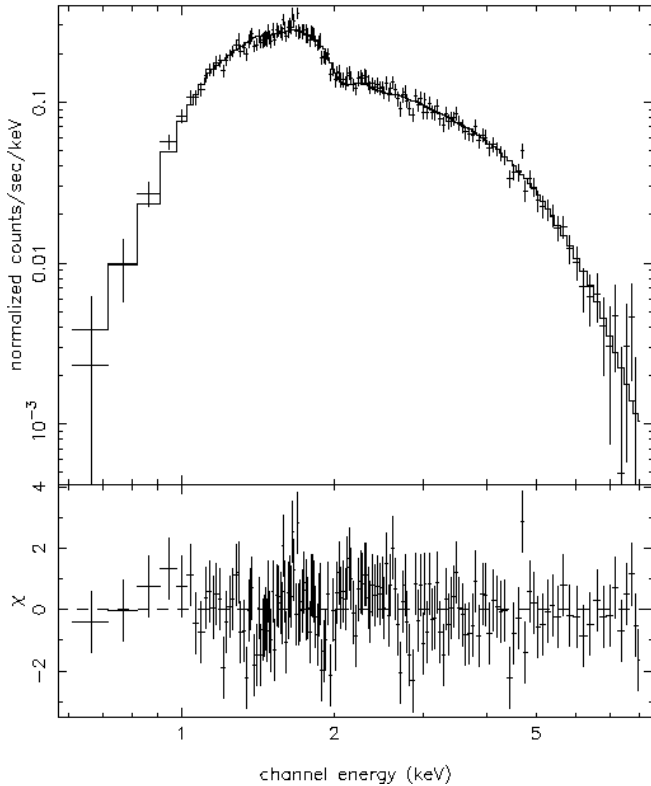


FIG. 7.—Spectra of the extended component (50''–150'') fitted with a power-law model (left-hand panel) and the APEC thermal model assuming solar abundances (right-hand panel). We show that while a nonthermal model fits this component adequately, the thermal model fails. The parameters of the best fit (power law) are summarized in Table 1.

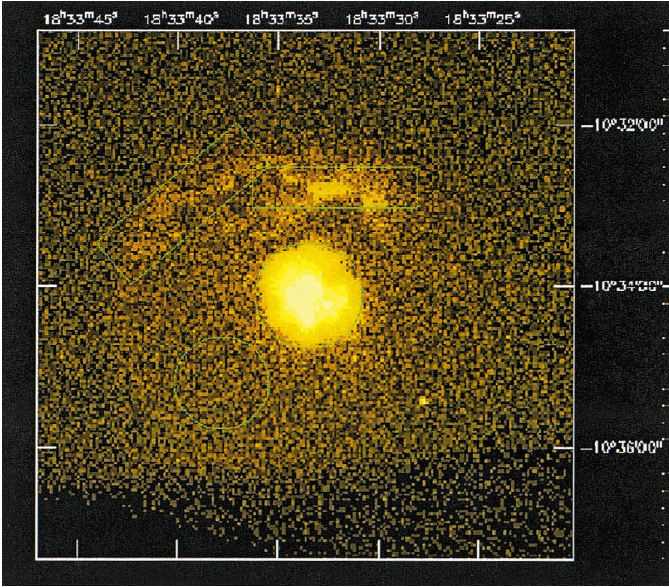


FIG. 8.—*Chandra* ACIS-S (0.5–10 keV) image of G21.5–0.9 showing the inner core ($R \sim 40''$) and the diffuse component extending out to a radius of $R \sim 2''.5$. We also show the regions selected for the spectral analysis (green): the northeastern knots, the brightest northwestern edge, and the southeastern region.

The selected regions are shown in Figure 8 (north is up, and east is to the left), and their corresponding spectra (in the 0.5–8.0 keV) are shown in Figure 9. There is no evidence of line emission. All the spectra are well fitted with a power-law model with $N_{\text{H}} = 1.9 \times 10^{22} \text{ cm}^{-2}$ (tied for the three spectra) and $\Gamma = 2.14, 2.19$, and 2.5 for the northern knots, the northeastern edge, and the southeastern region, respec-

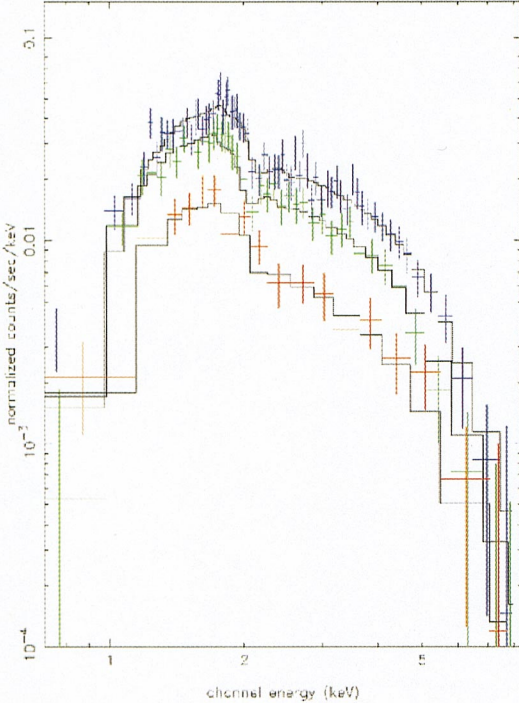


FIG. 9.—Data and the fitted power-law models for selected regions from the extended component, shown in Fig. 8. The blue, green, and red colors correspond to the bright northeastern knots, the northwestern edge, and the southeastern region, respectively.

tively ($\chi^2 = 0.50, v = 416$). The spectrum of the northern quadrant seems to have a harder spectrum than the rest of the diffuse emission. This result is in agreement with the hardness ratio map shown in Figure 2.

4.2. ROSAT PSPC

The source spectrum of the inner core is extracted from a circle of radius $R = 40''$. This defines the extent of the plerion seen with *ROSAT* (Fig. 3). When fitting the PSPC spectrum in the 0.1–2.4 keV range with a power-law model, we get $N_{\text{H}} = 1.95(1.35–2.74) \times 10^{22} \text{ cm}^{-2}$, $\Gamma = 1.95$ (0.5–3.8), and $\chi^2_v = 0.95$ ($v = 75$). The error bars are large because of the poor statistics and the narrow energy band of *ROSAT*. To better constrain the parameters, we fit the *ROSAT* PSPC (0.1–2.4 keV) spectrum simultaneously with the ACIS-S (0.5–10 keV) spectrum extracted from the 40'' radius core. The power-law model yields $N_{\text{H}} = 2.23(2.22–2.76) \times 10^{22} \text{ cm}^{-2}$, $\Gamma = 1.85$ (1.83–1.87), and $\chi^2_v = 1.1$ ($v = 889$). The total observed flux from the inner core is $5 \times 10^{-11} \text{ ergs cm}^{-2} \text{ s}^{-1}$, which translates to an unabsorbed luminosity $L_{\text{x}} = 2.8 \times 10^{35} \text{ ergs s}^{-1}$ (at a distance of 5 kpc). The data and fitted model are shown in Figure 10.

4.3. Comparison with ASCA Archival Data

We here present the analysis of the *ASCA* archival data in order to compare *ASCA* and *Chandra* spectra. While *ASCA* has a much poorer angular resolution than *Chandra*, its spectral resolution is comparable to that of the ACIS-S3 chip. *ASCA* has the advantage over *EXOSAT* and *Ginga* in better determining the average photon index of the plerion. This was noted by Gallant & Tuffs (1998), who found that extrapolating from X-rays to the infrared wavelengths using the photon index determined with *EXOSAT* and *Ginga* yields fluxes lying well below the measured ISOCAM values.

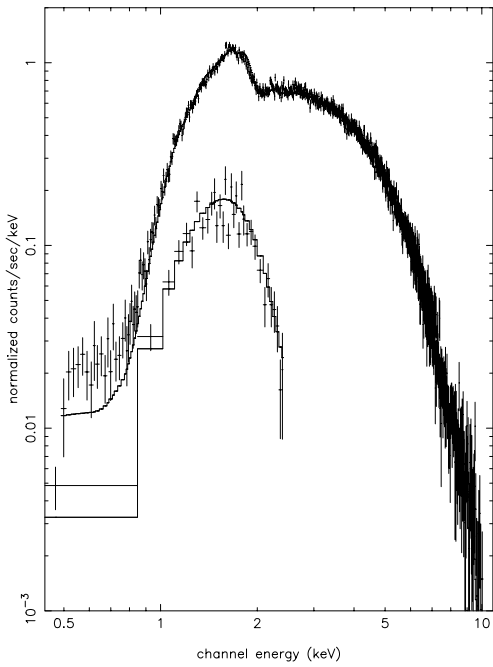


FIG. 10.—PSPC and ACIS-S3 spectra of the inner 40'' core fitted with a power-law model (§ 4.2).

We have extracted the *ASCA* spectra from a circular region of radius $R = 3'$, centered at the maximum of emission [R.A. (J2000) = $18^{\text{h}}33^{\text{m}}33\overset{\text{s}}{.}5$, decl. (J2000) = $-10^{\circ}34'3\overset{\text{s}}{.}1$]. We chose a region of $3'$ radius since the source is $7\overset{\text{s}}{.}25$ offset from the telescope axis and a larger extraction radius would include events from the edge of the detectors. Since G21.5-0.9 is located in the Galactic bulge region, we performed the background subtraction using a region from the same field of view. This has the advantage of minimizing the contamination of the source spectra by the high-energy emission from the Galactic ridge.

We combine the spectra from the SIS and GIS detectors and fit them simultaneously by introducing a relative normalization between the SIS and the GIS spectra. A power-law model yields an adequate fit with an interstellar absorption $N_{\text{H}} = 2.06(2.0\text{--}2.12) \times 10^{22} \text{ cm}^{-2}$, a photon index $\Gamma = 1.89$ (1.85–1.93), and $\chi^2_v = 0.98$ ($v = 755$). The observed flux in the 0.5–10 keV range is $7.6 \times 10^{-11} \text{ ergs cm}^{-2} \text{ s}^{-1}$, which translates to an unabsorbed luminosity $L_{\text{X}}(0.5\text{--}10 \text{ keV}) = 4.3 \times 10^{35} \text{ ergs s}^{-1}$ (at a distance of 5 kpc). The derived photon index of 1.9 is steeper than that derived with *EXOSAT* (Davelaar et al. 1986) and is closer to the value of 2.0 required by Gallant & Tuffs (1998) to account for the measured infrared fluxes. The small discrepancy might be due to the contamination of the ISOCAM fluxes by emission lines or to the subtraction of stellar contribution (Y. Gallant 2001, private communication).

5. TIMING

To search for pulsations in the *ASCA* data, we extract the events from an aperture of radius $3'$ in the GIS images. The GIS data were obtained in the high bit rate mode, with a photon time-of-arrival (TOA) resolution of 0.061 ms. We perform a power spectral density analysis on the barycenter-corrected photon arrival times using the hard band (2–10 keV). No significant pulsations were found. The failure to detect pulsations could be partly attributed to the contamination of the extracted events by the plerion. The analysis of the *Chandra* ACIS-S3 image indicates that only $\sim 20\%$ of the counts collected in the $3'$ *ASCA* GIS PSF originate from the central $5''$ radius circular region (in the 2–10 keV band).

We have also searched for pulsations in the *Chandra* HRC data. Slane et al. (2000) analyzed one HRC-I set (ObsID 1406) and obtained an upper limit of 40% on the

pulsed fraction of the central source. By the time of our analysis, there were 11 HRC observations in the public archive. We use only five of them (Table 2): two sets acquired with the HRC-S and three sets with HRC-I. The rest of the HRC observations were observed with large $\pm Y$ offsets,¹¹ which led to considerable spread of the source profile or contained serious processing errors (ObsID 1298). Various parameters of the analyzed sets (including the time spans T_{span} and the effective exposures T_{exp}) are presented in Table 2. All the data were obtained with nonoptimal focus positions (see parameter SIM_X in Table 2), which led to broadening of the core. For each of the five sets, a short period of time at the start of the exposure was excluded from consideration because of an unstable count rate. The total time span for all the observations (September 4–February 15) amounted to 14,328 ks, with 75.731 ks total effective exposure time.

The HRC-I data were filtered making use of the HRC screening algorithm.¹² The TOAs were converted to barycentric dynamic times (TDBs) with the “aXbary” task of CIAO. We extracted the events for the timing analysis from the apertures of 15 pixel ($\approx 2''$) radius centered at the core position; the numbers of counts are given in Table 2. The event count rate in set 143 is lower than in the other sets because its higher background count rate saturated telemetry.

Because of a wiring error in the HRC detector,¹³ the TOA ascribed to an event in a data file is actually the TOA of the following event, which may be a photon event or, more likely, a background particle event not telemetered to the ground. Therefore, a typical TOA error is equal to the average time between the successive events in the HRC detector, including the particle events. Making use of the level 0 supplementary data products, which contain the total (photon + particle) count rates for the whole HRC detector, we estimated the mean errors of about 5 ms for all the sets except for 143, for which the error is about 1 ms. In principle, the errors could be reduced by additional filtering of the extracted events, retaining only events such that the time to the next recorded event is less than a given value. This filtering, however, strongly reduces the number of

¹¹ See <http://asc.harvard.edu/udocs/docs/POG/MPOG/index.html>.

¹² See <http://asc.harvard.edu/cal/Links/Hrc/CIP/filter.html>.

¹³ See <http://asc.harvard.edu/hrc/timing.html>.

TABLE 2
Chandra/HRC OBSERVATIONAL SETS

Observation ID	Detector	Date	Epoch ^a (MJD)	T_{span} ^b (s)	T_{exp} ^c (s)	SIM_X ^d (mm)	N^e
143	HRC-I	1999 Sep 4	51,425.339	15243	15243	-1.0160	179
1242	HRC-I	1999 Sep 4	51,425.524	14855	14855	-1.0160	555
147	HRC-S	1999 Sep 5	51,426.625	9747	9747	-1.3705	496
1406 ^f	HRC-I	1999 Oct 25	...	27572	25621	-1.0389	...
1406A	51,476.316	13797	543
1406b	51,476.475	13726	590
146	HRC-S	2000 Feb 16	51,591.026	10334	10265	-1.4282	518

^a Epoch refers to the central time of the exposure.

^b Time span.

^c Effective exposure time.

^d Focus position along the telescope axis; the optimal positions are -1.04 mm for HRC-I and -1.53 mm for HRC-S.

^e Number of counts used in the analysis.

^f The 1406 set was divided in two parts; see explanations in § 5.

events available for the analysis, so it is not applicable in our case because of the small number of photons. Therefore, the timing errors force us to choose a minimum period considerably longer than 5 ms (maximum frequency smaller than 200 Hz). We chose the frequency range $0.01 \text{ Hz} < f < 50 \text{ Hz}$.

The presence of several data sets allows us to use the “correlated periodicity search” (Pavlov, Zavlin, & Trümper 1999). For each of the data sets, we use the Z_1^2 (Rayleigh) test (Buccheri et al. 1983). The function $Z_1^2(f)$ has numerous peaks, with characteristic widths $\delta f \approx T_{\text{span}}^{-1}$. One of these peaks may correspond to the pulsar frequency; the others are caused by statistical noise. If there is the pulsar peak at a frequency f_0 in one of the data sets, it should also be seen in each of the other sets, at frequencies $f_0 + \dot{f}_0 \Delta T$, where \dot{f}_0 is the pulsar frequency derivative and ΔT is the time between the corresponding observations. To identify the true pulsar peak (i.e., to find f_0 and \dot{f}_0), we choose a reference data set and examine the highest peaks in this set for the presence of counterpart peaks in the other sets for a reasonable range of \dot{f} . If no counterpart peaks are found in at least one of the data sets, we have to conclude that the peak under examination is due to statistical noise. If counterpart peaks are found in all the sets, they must satisfy some statistical criteria to be considered viable candidates for the pulsar peaks (see A. B. Koptsevich & G. G. Pavlov 2001, in preparation, for a description of the algorithm).

For the frequency derivative range, we choose $-1 \times 10^{-9} \text{ Hz s}^{-1} < \dot{f} < 0 \text{ Hz s}^{-1}$, which includes the \dot{f} values for all the known rotation-powered pulsars. All the sets, except for 1406, meet the requirement $|\dot{f}|_{\text{max}} T_{\text{span}}^2 / 2 \ll 1$, which allows us to consider Z_1^2 as independent of \dot{f} for each of these sets. To make the computations uniform, we divide set in two successive subsets, 1406A and 1406B (see Table 2), which satisfy this requirement.

We applied this approach to the six data sets and found no statistically significant periodicity. The series of highest peaks found in all the six sets corresponds to ephemeris parameters $f = 47.7154362408 \text{ Hz}$ and $\dot{f} = -6.60 \times 10^{-10} \text{ Hz s}^{-1}$ (epoch 51,425.25047454 MJD TDB). Combining the six sets in one, we find a Z_1^2 value of 36.6 for these values of f and \dot{f} . The probability to find such a peak is close to unity, so that the result is statistically insignificant. The corresponding pulsed fraction for a sinusoidal signal, $f_p = (2Z_1^2/N)^{1/2} = 16\%$ (where $N = 2881$ is the total number of events), coincides with that measured from the extracted light curve ($15\% \pm 5\%$) and can be considered as an upper limit. This is considerably smaller than the limit derived by Slane et al. (2000).

6. DISCUSSION

We have presented archival X-ray observations of G21.5–0.9 with *Chandra*, *ROSAT*, and *ASCA*. The spectrum of G21.5–0.9 is nonthermal and best fitted with a power-law model, whose index steepens by $\Delta\Gamma \sim 1$ from the central part of the remnant to the outer component (at $\sim 150''$). The total unabsorbed flux from the 5' diameter SNR is $F_X(0.5\text{--}10 \text{ keV}) = 1.1 \times 10^{-10} \text{ ergs cm}^{-2} \text{ s}^{-1}$ with an 85% contribution from the 40" radius core. At a distance of 5 kpc, this translates to a total luminosity $L_X(0.5\text{--}10 \text{ keV}) = 3.3 \times 10^{35} \text{ ergs s}^{-1}$. The low surface brightness extended component discovered with *Chandra* does not have the limb-brightened morphology expected from an SNR blast wave or shocked ejecta. It has rather a filled

morphology, with knots and filaments most evident in the northern quadrant. There is no significant evidence of thermal emission lines from this component. Based on the morphology and the spectrum of this component, we conclude that it is an extension of the inner core and that the filaments could be plerionic “wisps,” as seen in Crab-like plerions. We note that *XMM-Newton* has recently observed G21.5–0.9 (Warwick et al 2001), and the results agree with our findings. In this paper, we have investigated in more detail the spectral variations across the remnant on smaller scales and determined a more stringent upper limit on the pulsed fraction. We have also presented for the first time the results from the *ROSAT* and *ASCA* observations as a consistency check for the overall spectral analysis. We show that only the nonthermal model fits to the extended component (with *Chandra*) yield a column density consistent with that found for the core, whereas the thermal models (CEI or NEI) yield a much lower N_{H} value.

In the following sections, we use our spectral and timing results to determine the parameters of the plerion and a “hidden” pulsar. By comparing the *Chandra* ACIS image with the radio image, we conclude that the morphology of G21.5–0.9 could be associated with a pulsar wind and possibly jets interacting with the surroundings. The failure to detect pulsations could be due to a geometrical effect. We estimate the parameters of the putative pulsar in G21.5–0.9 plerion and compare them with those derived for the well-studied Crab and 3C 58 nebulae. Finally, the absence of thermal emission in G21.5–0.9 could be due to a low-density medium or a cavity in which the supernova explosion occurred.

6.1. Distance

To estimate the distance to G21.5–0.9, we regard the N_{H} values found from the ACIS fits and those from the *ASCA* and *ROSAT* fits to describe a reasonable range of possible N_{H} values, $(1.8\text{--}2.3) \times 10^{22} \text{ cm}^{-3}$. This range encompasses the values from all the global power-law fits and excludes the considerably different values required for thermal fits. The extinction per unit distance in the direction of G21.5–0.9 can be estimated from the contour diagrams given by Lucke (1978): $\langle E_{B-V} \rangle / D \sim 0.8 \text{ mag kpc}^{-1}$. Using the relation $\langle N_{\text{H}} / A_V \rangle = 1.79 \times 10^{21} \text{ cm}^{-2} \text{ mag}^{-1}$, which translates into $\langle N_{\text{H}} / E_{B-V} \rangle = 5.55 \times 10^{21} \text{ cm}^{-2} \text{ mag}^{-1}$ (Predehl & Schmitt 1995), we derive a distance of 4.1–5.2 kpc. This range is consistent with the lower estimate on D obtained from 21 cm absorption (Becker & Szymkowiak 1981). In the following, we assume a distance of 5 kpc and express our results as functions of $D_5 = D/(5 \text{ kpc})$.

6.2. The Putative Pulsar

The morphology and spectrum of the inner core indicate the presence of a pulsar powering G21.5–0.9. The failure to detect pulsations could be due to a beaming effect. We note that 3C 58 is another Crab-like plerion whose properties hint at the presence of a pulsar, yet no pulsar has been found there (Torii et al. 2000). To estimate the spin-down energy loss of the pulsar \dot{E} one can use an empirical relationship connecting \dot{E} and the X-ray luminosity L_X for pulsar-powered plerions. For instance, using the formula by Seward & Wang (1988), $\log L_X = 1.39 \log \dot{E} - 16.6$, where L_X is the luminosity of the pulsar plus plerion in the 0.2–4 keV band, we get $\dot{E} = 2.7 \times 10^{37} D_5^{1.44} \text{ ergs s}^{-1}$. Using $L_X = 3 \times 10^{-11} \dot{E}^{1.22} \text{ ergs s}^{-1}$ (Slane et al. 2000) and a total

luminosity (inner core + extended component) of $3.3 \times 10^{35} D_5^2$ ergs s $^{-1}$ in the 0.5–10 keV band, we estimate $\dot{E} = 5.5 \times 10^{37} D_5^{1.64}$ ergs s $^{-1}$. Thus, a plausible estimate for the spin-down energy loss is $\dot{E}_{37} \equiv \dot{E}/(10^{37} \text{ ergs s}^{-1}) \sim 3\text{--}6$.

We can now use this \dot{E} and a plausible age of G21.5–0.9 to estimate the parameters of the putative pulsar powering G21.5–0.9. The age of G21.5–0.9 is rather uncertain—various estimates range from 0.8 to 40 kyr (Salter et al. 1989; Fürst et al. 1988; Morsi & Reich 1987). The linear size of the X-ray plerion in G21.5–0.9 is $\sim 3.6 D_5$ pc diameter, slightly bigger than that in the Crab and 3C 58 nebulae. The ratio L_X/\dot{E} for G21.5–0.9 is $\sim 0.006\text{--}0.011$. This is smaller than those for the 1000 yr old plerions around the Crab pulsar and PSR 0540–69 (0.05), and it is comparable with $L_X/\dot{E} \approx 0.01$ for the plerion associated with the 1500 yr old pulsar, PSR 1509–58 in the SNR MSH 15–52 (Chevalier 2000). On the other hand, the known pulsars with $\dot{E}_{37} \sim 3\text{--}6$ have characteristic ages τ in a range of 1.5–10 kyr. In the following analysis, we normalize the pulsar parameters to $\tau_3 = \tau/(3 \text{ kyr})$.

Given \dot{E} and τ , the period P of a pulsar can be estimated as

$$P = \left[\frac{4\pi^2 I}{(n-1)\dot{E}\tau} \right]^{1/2} = 0.144 \left(\frac{2}{n-1} \right)^{1/2} \left(\frac{I_{45}}{\dot{E}_{37}\tau_3} \right)^{1/2} \text{ s}, \quad (1)$$

where n is the braking index ($\dot{P} = KP^{2-n}$), $\tau = P/[(n-1)\dot{P}] = t + \tau_0$, t is the true age, $\tau_0 = P_0/[(n-1)\dot{P}_0]$, P_0 and \dot{P}_0 are the initial period and its derivative, respectively, and $I = 10^{45} I_{45}$ g cm 2 is the moment of inertia. In this model, $\tau \approx t$ if $t \gg \tau_0$, which is equivalent to $P \gg P_0$. The corresponding period derivative is $\dot{P} = P/[(n-1)\tau] = 7.6 \times 10^{-13} [2/(n-1)]^{1/2} I_{45}^{1/2} \dot{E}_{37}^{-1/2} \tau_3^{-3/2}$. Assuming $n = 3$ (magneto-dipole braking), we can estimate the conventional magnetic field, $B = 3.2 \times 10^{19} I_{45}^{1/2} R_{10}^{-3} (P\dot{P})^{1/2} = 3.2 \times 10^{13} I_{45}^{1/2} \dot{E}_{37}^{-1/2} \tau_3^{-1} R_{10}^{-3}$ G, where $R = 10R_{10}$ km is the neutron star radius. The inferred magnetic field is comparable to those of very young radio pulsars.

The X-ray luminosities $L_X^{(p)}$ of the radio pulsars detected with *ROSAT* (0.1–2.4 keV band) show strong correlation with the value of \dot{E} , which allows us to estimate the X-ray luminosity of the putative pulsar in G21.5–0.9. Using the relationship derived by Ögelman (1995), $L_X^{(p)} \sim 6.6 \times 10^{26} (B_{12}/P^2)^{2.7}$ ergs s $^{-1}$, which is equivalent to $L_X^{(p)} = 1.5 \times 10^{-16} \dot{E}_{37}^{1.35}$ ergs s $^{-1}$, we obtain $L_X^{(p)} = 1.3 \times 10^{34} \dot{E}_{37}^{1.35}$ ergs s $^{-1}$. The formula suggested by Becker & Trümper (1997), $L_X^{(p)} = 10^{-3} \dot{E}$, gives approximately the same value, $L_X^{(p)} = 1 \times 10^{34} \dot{E}_{37}$ ergs s $^{-1}$. We can now compare these values with an observed upper limit on the pulsar flux. To estimate a conservative upper limit, we measure the flux in a 0.5' radius aperture placed at the brightest part of the core (see Fig. 5). We normalize the PSF to match the number of counts in the central 0.5' bin. We then estimate the ratio of counts within 0.5' to counts within 1" radius and scale their corresponding fluxes accordingly. Using the estimated flux of 3.5×10^{-12} ergs cm $^{-2}$ s $^{-1}$ from the 1" central core (§ 4.1), we estimate an unabsorbed flux of 2.4×10^{-12} ergs cm $^{-2}$ s $^{-1}$ from the point source. This translates to an upper limit on the flux from a hidden pulsar of 1.1×10^{-12} ergs cm $^{-2}$ s $^{-1}$ in the 0.1–2.4 keV range (assuming $\Gamma = 1.5$). If the pulsar's X-ray emission were isotropic, the corresponding upper limit on the pulsar luminosity would be $L_X^{(p)} < 3.5 \times 10^{33} D_5^2$ ergs s $^{-1}$, an order of magnitude lower than the above predictions based on the \dot{E}

estimates. This indicates that the X-ray radiation of the pulsar is strongly beamed and that the orientation of the pulsar's rotation and magnetic axes is such that the rotating beam does not come close to the line of sight, in agreement with the lack of observable pulsations.

6.3. Pulsar Wind Model

In the Kennel & Coroniti (1984, hereafter KC 84) model, a pulsar injects high-energy particles in the form of a relativistic particle wind. Confinement of the pulsar wind by its surroundings causes the outflow to decelerate at a shock, forming a synchrotron nebula. The radius of the shock R_s is given by equating the pressure of the pulsar's wind $\dot{E}/(4\pi R_s^2 c)$ with the pressure in the nebula P_n . Beyond this radius, a nonrelativistic flow transports the plasma from the shock region to the edge of the nebula. The size of the nebula R_n is related to the shock radius R_s as $R_n/R_s \sim 1/\sigma^{1/2}$, where σ is the so-called pulsar wind magnetization parameter defined as the ratio of the Poynting flux to the particles flux (KC 84). Self-consistent models for the Crab nebula require that the wind is particle dominated; i.e., σ is small ($\leq 10^{-2}$; KC 84). From the *ROSAT* PSPC and *Chandra* ACIS-S spectra, we estimate an equipartition magnetic field $B_{eq} = 1.8 \times 10^{-4}$ G in the 40" radius core. This yields a pressure in the inner 40" radius core of $B^2/8\pi \sim 1.29 \times 10^{-9}$ ergs cm $^{-3}$ and therefore $R_s = 0.046 \dot{E}_{37}^{0.5}$ pc. Using the estimated $\dot{E}_{37} \sim 3\text{--}6$ (§ 6.2), we get $R_s \sim 0.08\text{--}0.11$ pc, which corresponds to an angular size of $\sim 3''\text{--}5''$ (at 5 kpc). Using the nebular size $R_n \sim 150''$, we estimate the pulsar wind parameter $\sigma \sim (R_s/R_n)^2 \sim (4\text{--}11) \times 10^{-4}$, indicating a particle dominated wind—like the Crab and the other Crab-like nebulae. In Table 3, we summarize the inferred parameters of the putative pulsar in G21.5–0.9, in comparison with the Crab pulsar and the putative pulsar in 3C 58. When fitting the spectra in circular rings of G21.5–0.9, we have found that the photon index steepens away from the center all the way out to a radius of 150"—a result expected from synchrotron losses. Chevalier (2000) has developed a one-zone, shocked wind model to model the X-ray luminosity of pulsar nebulae. This model is a simplified version of the KC 84 model, and predicts that the average spectral index of the whole pulsar wind nebula is 0.5 steeper than that of the core. This is roughly consistent with our result. However, the small scale spatial variations of the photon index in the nebula (Γ varying from 1.5 in the innermost 5" core to 2.7 in the extended component)

TABLE 3
COMPARISON OF THE PARAMETERS OF THE PUTATIVE PULSAR
IN G21.5–0.9 WITH THE CRAB PULSAR AND THE PUTATIVE PULSAR
IN 3C 58

Parameter	G21.5–0.9	Crab	3C 58
Distance (kpc)	5	2	3.2
L_X^a (10^{35} ergs s $^{-1}$)	$3.3D_5^2$	210	0.2
\dot{E} (10^{37} ergs s $^{-1}$)	3–6	47	0.4
σ^b	$(4\text{--}11) \times 10^{-4}$	3×10^{-3}	$\sim 6 \times 10^{-3}$
P^c (ms)	$144\tau_3^{-0.5} \dot{E}_{37}^{-0.5}$	33	440
B_0 ($\times 10^{13}$ G)	$1.1\tau_3^{-1} \dot{E}_{37}^{-0.5}$	0.4	6

^a X-ray luminosity of the plerion in the 0.5–10 keV range.

^b Pulsar wind parameter defined as the ratio of the Poynting flux to the kinetic energy flux (KC 1984).

^c The following notations are used: τ_3 is the age of the SNR in units of 3 kyr, \dot{E}_{37} is the spin-down energy loss in units of 10^{37} ergs s $^{-1}$, and D_5 is the distance in units of 5 kpc.

need to be examined with spatially resolved models (R. A. Chevalier 2001, private communication).

6.4. Correlation with the Radio Image

The high-resolution 22.3 GHz radio image of G21.5–0.9, obtained with the NRO Millimeter Array, shows a diffuse centrally peaked component plus axisymmetric filaments (Fürst et al. 1988). The authors suggest that the symmetry in the lobes is evidence of precessing jets from a hidden pulsar. In order to compare the radio image with our X-ray image, we scale the ACIS-S image to that of the radio image (Fig. 7 in Fürst et al. 1988) and show the resulting image in Figure 11. The left-hand panel shows the 40'' radius inner core of G21.5–0.9, binned to the same scale, smoothed with a Gaussian with $\sigma = 3''$, and with the contours overlaid. The right-hand panel shows the radio image of the core with the jets model proposed by Fürst et al. (1988). It is clear that the X-ray trough in the northwest is strongly correlated with that of the radio image. Our result therefore supports the proposed picture. It is interesting that the shock radius ($R_s \sim 0.1$ pc; § 6.3) coincides with the axisymmetric filaments seen in the radio (Fürst et al. 1988). Therefore, those structures could be due to the deceleration of the pulsar wind (or jets) confined by the nebular pressure. They also found that the polarization varied from the center to the outer boundary, from almost zero to 20%–30%. They conclude that this is explained by a change in the magnetic field geometry, with little contribution from a radial field from the inner regions because of geometrical effects.

6.5. Where is the SNR Shell?

To date, we know ~ 10 Crab-like SNRs that lack an SNR shell that would be expected from the shocked ambient matter or shocked ejecta. The lack of SNR shells is still a puzzling issue, and many deep searches for shells around

the Crab nebula and 3C 58 have failed to find them. It has been suggested that the absence of a shell could be due to a propagation in a low-density medium (in which case the shell would be very faint) or to a low efficiency in accelerating particles and amplifying the magnetic field (Reynolds & Aller 1985). A deep search in the radio for the G21.5–0.9 shell is needed since all current radio observations have been performed to study mainly the bright inner core. Slane et al. (2000) suggested that the extended component is associated with the blast wave of the supernova explosion or from the shocked ejecta. Here we rule out thermal CEI models. Fitting with NEI models, which are more realistic to model thermal emission from young SNRs, indicates unusually low abundances or unusually low ionization timescales. Furthermore, the derived N_{H} is inconsistent with that derived for the SNR. We find no evidence of line emission in any part of the remnant, leading us to conclude that the spectrum is dominated by nonthermal emission.

A growing number of SNRs show evidence of nonthermal emission from their shells (e.g., SN 1006). The emission mechanism has been attributed to synchrotron radiation from high-energy particles accelerated at the SNR shock (Allen, Gotthelf, & Petre 1999). Reynolds & Chevalier (1981) have noted that the nonthermal spectra should not be described by a power law but rather a power law with a roll-off at high energies. If the nonthermal emission in the extended component of G21.5–0.9 is indeed due to synchrotron radiation from highly energetic particles accelerated at the SNR shock, then one would expect it to be fitted with the cutoff or escape models recently included in XSPEC Version 11.0, which are more appropriate for modeling nonthermal emission from SNR shells (Reynolds & Keohane 1999; Dyer et al. 2001). These models require knowledge of the radio flux density and the radio spectral index. With the absence of a radio counterpart, we fit the

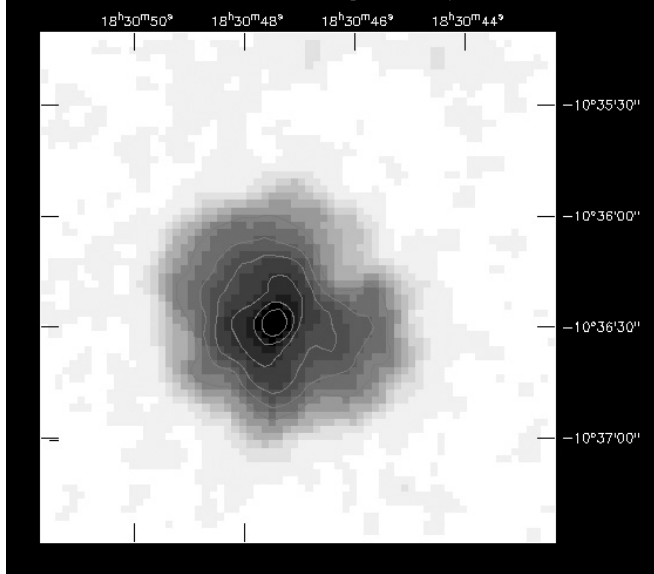
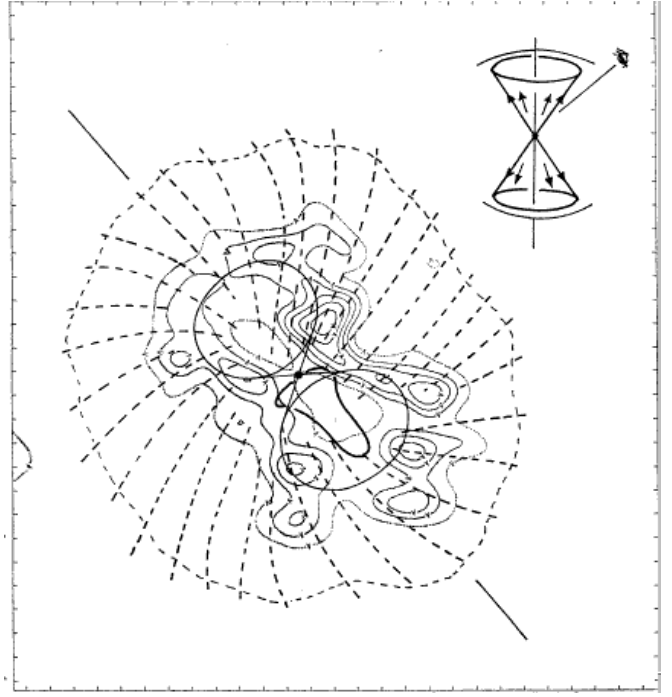


FIG. 11.—ACIS-S and 22.3 GHz images of G21.5–0.9, binned to the same scale (B1950 coordinates). The morphology of the plerion in X-rays follows the enhancements seen in the filamentary radio structures.



X-ray spectrum with the “sresc” model, leaving these parameters free. This model does not provide a good fit ($\chi^2_v = 1.36$, $v = 670$). This again argues against a shell interpretation for the extended component.

The nonthermal emission in the extended component is most likely due to synchrotron emission from particles accelerated and injected by the hidden pulsar. Using the power-law model parameters of the extended component (Table 1, first row) and assuming equipartition of particles and magnetic field, we estimate an equipartition field of 1.8×10^{-4} G. The lifetime of the synchrotron emitting electrons is only $60 E_{\gamma, \text{keV}}^{-0.5} B_{-4}^{-1.5}$ yr, where $E_{\gamma, \text{keV}}$ and B_{-4} are the photon’s energy in units of 1 keV and the magnetic field in units of 10^{-4} G, respectively. The synchrotron lifetime is much smaller than the estimated age of the SNR—a result also found in the Crab and Crab-like nebulae. The electrons can propagate out to a radius of 3 pc if they are traveling at a speed of $0.15cE_{\gamma, \text{keV}}^{0.5} B_{-4}^{1.5}$. The enhancement of brightness in the northwest quadrant could be due to the propagation into a denser medium (as is evident in the public IRAS images of G21.5–0.9). To get an upper limit on the density of the ambient medium, we fit the extended component with a power-law plus a thermal model (APEC). We freeze the power-law model parameters to their best value (Table 1) and determine an upper limit on the emission measure (EM) of the thermal component. We get $\text{EM} \leq 1.1 \times 10^{-4}$ (at the 90% confidence level). Using $\text{EM} = 10^{-14}(4\pi D^2)^{-1} \int n_e n_H dV$, where n_e and n_H are the post-shock electron and hydrogen density, respectively, and V is the volume of the extended component, we estimate $\langle n_e n_H \rangle^{1/2} \leq 0.07 D_5^{-1/2} \text{ cm}^{-3}$. Assuming a strong shock with compression ratio 4, the ambient density n_0 is $\leq 0.02 D_5^{-1/2} \text{ cm}^{-3}$.

G21.5–0.9 is perhaps most similar to the plerionic SNR 3C 58, although there are some differences. Both plerions have a morphology hinting at the presence of a pulsar yet undetected. They both have a low-frequency spectral break (at 50 GHz) and thus belong to the class of plerions of the second kind (Salvati et al. 1998). Woltjer et al. (1997) suggest that these plerions are powered by short-lived pulsars with either very small braking indices or pulsars that would undergo a phase change in the pulsar’s energy output. Both are young and exhibit a bright inner core plus a fainter extended component whose spectra are dominated by non-thermal emission. The extended component in 3C 58 shows, however, a small flux (6% of the total) of thermal nature, which was attributed to the expansion of the outer rim into inner ejecta core (Bocchino et al. 2001). G21.5–0.9 is also similar to the Crab nebula in that it has a centrally filled morphology and a nonthermal spectrum. The softening of the spectral index away from the center in G21.5–0.9 is similar to that in the Crab nebula (Willingale et al. 2001). In spite of these similarities, G21.5–0.9 remains a unique plerion. Its X-ray brightness profile (core + plateau) and its morphology are puzzling and cannot be explained by diffusion models such as Becker (1992). The detection of axisymmetric filaments in the radio and X-rays hint at a complex magnetic field geometry and/or jet structures (Warwick et al. 2001).

The most unusual property of G21.5–0.9 plerion lies in the radio regime. Plerions are usually bigger in size at lower energies since the high-energy photons have a shorter lifetime than the low-energy photons. Therefore, one would expect to see a bigger plerion in the radio. This is the case for the Crab nebula. In 3C 58, there is a close correspondence between the radio morphology of the outer nebula and the X-ray map at soft energies (Bocchino et al. 2001). For G21.5–0.9, only the inner 40'' radius core has been detected in the radio. Slane et al. (2000) have put an upper limit on the 1 GHz surface brightness of the extended component of $\Sigma = 4 \times 10^{-21} \text{ W m}^{-2} \text{ Hz}^{-1} \text{ sr}^{-1}$. B. Gaensler (2000, private communication) has recently found a radio knot coincident with the hard X-ray brightest knot/filament found in the northern region. A deep observation of G21.5–0.9 in the radio and at the short wavelengths (currently conducted with the VLA) will determine the spectral characteristics of this knot and will allow us to search for the radio counterpart of the extended component and the missing SNR shell.

We note that since G21.5–0.9 is bright and heavily absorbed, a significant fraction of the emitted X-rays will interact with dust and will be scattered (R. Smith 2001, private communication). Modeling a dust scattering X-ray halo (e.g., Smith & Edgar 2001) needs to be performed for this remnant. Finally, we note that a 65 ms pulsar has been very recently discovered in 3C 58 (Murray et al. 2001 implying a higher \dot{E} and a lower magnetic field than previously thought (see Table 3). This discovery strengthens the uniqueness of G21.5–0.9 and the urge to search for an underlying pulsar.

This research has made use of the HEASARC database and the NASA Astrophysics Data System (ADS). We are grateful to the Center for Academic Computing of the Pennsylvania State University for the opportunity to use the LION-X cluster¹⁴ for the period search. We thank Keith Arnaud (GSFC) for his help with XSPEC and *Chandra* software, Glenn Allen (MIT) for his help with ACIS issues at the early stages of writing this paper, Slava Zavlin (MPE) for useful discussions, Bryan Gaensler (MIT) for pointing out the finding of a radio knot in the extended component, and Yves Gallant (CEA, Saclay) for his input on the infrared emission from G21.5–0.9 and Randall Smith (CFA) for discussions about dust scattering halos. We also thank the referee for careful reading and useful comments. S. S. H. acknowledges support by a NASA LTSA grant through the cooperative agreement NCC5-356 with Universities Space Research Association (USRA), and by the Natural Sciences and Engineering Research Council (NSERC) at the University of Manitoba.

¹⁴ See <http://cac.psu.edu/beatnic/Cluster/Lionx/lionx.html>.

REFERENCES

- Allen, G. E., Gotthelf, E. V., & Petre, R. 1999, Proc. 26th Int. Cosmic-Ray Conf. (Salt Lake City), 3, 480
- Asaoka, I., & Koyama, K. 1990, PASJ, 42, 625
- Becker, P. A. 1992, ApJ, 397, 88
- Becker, R. H., & Szymkowiak, A. E. 1981, ApJ, 248, L23
- Becker, W., & Trümper, J. 1997, A&A, 326, 682
- Bocchino, F., Warwick, R. S., Marty, P., Lumb, D., Becker, W., & Pigot, C. 2001, A&A, 369, 1078
- Borkowski, K. J., Lyerly, W. J., & Reynolds, S. P. 2001, ApJ, 548, 820
- Buccheri, R., et al. 1983, A&A, 128, 245
- Chevalier, R. A. 2000, ApJ, 539, L45
- Davelaar, J., Smith, A. B., & Becker, R. H. 1986, ApJ, 300, L59
- Dyer, K. K., Reynolds, S. P., Borkowski, K. J., & Petre, R. 2001, ApJ, 551, 439
- Fürst, E., Handa, T., Morita, K., Reich, P., Reich, W., & Sofue, Y. 1988, PASJ, 40, 347
- Gallant, Y. A., & Tuffs, R. J. 1998, Mem. Soc. Astron. Italiana, 69, 963
- Kaspi, V. M., Manchester, R. N., Johnston, S., Lyne, A. G., & D'Amico, N. 1996, AJ, 111, 2028
- Kennel, C. F., & Coroniti, F. V. 1984, ApJ, 283, 710 (KC 84)
- Lucke, P. B. 1978, A&A, 64, 367
- Morsi, H. W., & Reich, W. 1987, A&AS, 69, 533
- Murray, S. S., Slane, P. O., Seward, F. D., Ransom, S. M., & Gaensler, B. M. 2001, preprint (astro-ph/0108489)
- Ögelman, H. B. 1995, in The Lives of Neutron Stars, ed. M. A. Alpar, Ü. Kiziloglu, & J. van Paradijs (NATO ASI series P, 116; Dordrecht: Kluwer), 101
- Pavlov, G. G., Zavlin, V. E., & Trümper, J. 1999, ApJ, 511, L45
- Predehl, P., & Schmitt, J. H. M. M. 1995, A&A, 293, 889
- Reynolds, S. P., & Aller, H. D. 1985, AJ, 90, 2312
- Reynolds, S. P., & Chevalier, R. A. 1981, ApJ, 245, 912
- Reynolds, S. P., & Keohane, J. W. 1999, ApJ, 525, 368
- Salter, C., Reynolds, S. P., Hogg, D. E., Payne, J. M., & Rhodes, P. J. 1989, ApJ, 338, 171
- Salvati, M., Bandiera, R., Pacini, F., & Woltjer, L. 1998, Mem. Soc. Astron. Italiana, 69, 1023
- Seward, F. D., & Wang, Z. 1988, ApJ, 332, 199
- Slane, P. O., Chen, Y., Schulz, N. S., Seward, F. D., Hughes, J. P., & Gaensler, B. M. 2000, ApJ, 533, L29
- Smith, R. K., & Edgar, R. J. 2001, in Two Years of Science with *Chandra*, in press
- Torii, K., Slane, P. O., Kinugasa, K., Hashimoto, K., & Tsunemi, H. 2000, PASJ, 52, 875
- Warwick, R. S., et al. 2001, A&A, 365, L248
- Weisskopf, M. C., O'dell, S. L., & van Speybroeck, L. P. 1996, Proc. SPIE, 2805, 2
- Willingale, R., Aschenbach, B., Griffiths, R. G., Sembay, S., Warwick, R. S., Becker, W., Abbey, A. F., & Bonnet-Bidaud, J.-M. 2001, A&A, 365, L212
- Woltjer, L., Salvati, M., Paciti, F., & Bandiera, R. 1997, A&A, 325, 295